Sensors and Materials, Vol. 37, No. 8 (2025) 3475–3487
MYU Tokyo

S & M 4130

Field-orientation-controlled Permanent Magnet Synchronous Motor Drive with Active Power Factor Correction

Yung-Chang Luo,* Zhi-Jie Hu, Wen-Yu Wang, and Wen-Cheng Pu

Department of Electrical Engineering, National Chin-Yi University of Technology,
No. 57, Sec. 2, Zhongshan Rd, Taiping Dist, Taichung 41170, Taiwan (ROC)

(Received December 27, 2024; accepted June 23, 2025)

Keywords: field orientation control (FOC), permanent magnet synchronous motor (PMSM) drive, active power factor correction (APFC), front-end bidirectional power flow converter, energy saving

An active power factor correction (APFC) front-end converter was developed for a field-orientation-controlled (FOC) permanent magnet synchronous motor (PMSM) drive. The decoupled FOC PMSM drive was designed on the basis of the stator current and flux to achieve the maximum torque-to-current ratio. Linear control was implemented for two-axis stator current controllers and a speed controller, with the stator current measured using Hall effect current sensors. The proposed bidirectional power flow front-end converter enables the FOC PMSM drive to maintain unity power factor operation in both motoring and regenerative braking modes, thereby enhancing power factor performance and promoting energy efficiency. The system was simulated using MATLAB/Simulink®, and all control algorithms were implemented on a Renesas RX62T microcontroller to generate pulse width modulation (PWM) signals for driving the APFC front-end converter and the PMSM. Both simulation and experimental results validated the effectiveness of the proposed method.

1. Introduction

Compared with induction motors, permanent magnet synchronous motors (PMSMs) offer several advantages, including high power density, high reliability, low losses, and compact size. These features align closely with the vision of sustainable environmental development by promoting low carbon emissions. Field orientation control (FOC) enables AC motors to emulate the characteristics of separately excited DC motors, providing ease of control and a high torque-to-current ratio. According to the FOC theory,[(1)] through coordinate transformation, the complex mathematical model of a PMSM can be decomposed into a torque-current component and a flux-current component, which are orthogonal to each other. By maintaining the rated flux and controlling the torque current, the maximum torque-to-current ratio can be achieved. The front-end AC-to-DC converter in conventional AC motor drives typically employs bridge rectification, which supports unidirectional power flow but introduces low-order harmonic currents into the power grid. This results in significant input current distortion, poor power factor, and degraded

*Corresponding author: e-mail: luoyc@ncut.edu.tw
https://doi.org/10.18494/SAM5529

ISSN 0914-4935

power quality. Improving the power quality of the front-end converter can be achieved through active and passive power factor correction (PFC) methods. Passive PFC utilizes passive components such as inductors and capacitors to construct a PFC circuit on the input side of the bridge rectifier. However, it is bulky and prone to resonance, and its harmonic current filtering capability is limited to a fixed bandwidth. Additionally, when the power supply is unbalanced, the transient response is poor. In contrast, a bidirectional power flow front-end converter employs voltage and current feedback compensation to control the switching state of the power switch module. This allows the boost inductor to either store or release energy, enabling active PFC (APFC). By making the input current track the reference current and maintain a sinusoidal waveform, phase correction is achieved: the voltage and current are in phase during motoring operation, and they are in opposite phases during regenerative braking. This method effectively improves the power factor of the FOC PMSM drive during both motoring and regenerative braking modes, and successfully addresses many of the limitations associated with conventional passive PFC methods. Various PFC front-end converters for AC motor drives have been published, including designs for induction motor drives with PFC front-end converters,[2–5] PFC front-end converters for brushless DC motor drives,[6–11] PMSM drives based on PFC front-end converters,[12–15] and switching reluctance motor drives with PFC front-end converters.[16–21]

In this research, a decoupled FOC PMSM drive was developed on the basis of the current and flux of the stator. Three-phase stator current measurements were obtained using electromagnetic Hall effect current sensors. The speed controller and the d^e-axis and q^e-axis stator current controllers of the FOC PMSM drive were designed using the pole placement method. A bidirectional power flow front-end converter with APFC was implemented by setting zero reactive power to achieve unity power factor operation. Grid voltage and current measurements were obtained using electromagnetic Hall effect current sensors and a voltage-dividing isolation sensor, respectively. The voltage and current control loops of the front-end converter were designed using root locus and Bode plot techniques. These methodologies demonstrated the successful implementation of an FOC PMSM drive with APFC, achieving both effective control and PFC.

This paper is organized into five sections. In Sect. 1, we present the research background and motivation, along with a review of the literature on FOC PMSM drives and APFC front-end converters. In Sect. 2, we describe the decoupled FOC PMSM drive system and the linear controller design, incorporating voltage feed-forward compensation. The development of an APFC bidirectional power flow converter, capable of achieving unity power factor operation during both motoring and regenerative braking, is detailed in Sect. 3. In Sects. 4 and 5, we discuss the simulation and experimental results, followed by the conclusions.

2. Decoupled FOC PMSM Drive

PMSM uses high-permeability permanent magnets instead of rotor windings as rotor poles without rotor copper losses, making it more efficient and reliable than other types of motor. The magnetic axis of the permanent magnet is consistent with the rotor shaft. The position angle of the synchronous reference frame can be obtained from the rotor shaft position, and then based on the FOC theory, the maximum torque-to-current ratio can be achieved.

PMSM utilizes high-permeability permanent magnets as rotor poles, eliminating the need for rotor windings and thereby avoiding rotor copper losses. This design enhances both efficiency and reliability compared with other types of motor. The magnetic axis of the permanent magnet aligns with the rotor shaft, and the position angle of the synchronous reference frame is determined from the rotor shaft position. Based on the FOC theory, this alignment allows for the achievement of the maximum torque-to-current ratio.

The two-axis stator voltage equations of a PMSM in the synchronous reference frame are given as[22]

$$R_s i_{ds}^e + p\lambda_{ds}^e - \omega_e \lambda_{qs}^e = v_{ds}^e , \tag{1}$$

$$R_s i_{qs}^e + p\lambda_{qs}^e + \omega_e \lambda_{ds}^e = v_{qs}^e , \tag{2}$$

where i_{ds}^e and i_{qs}^e are the d^e-axis and q^e-axis stator currents, v_{ds}^e and v_{qs}^e are the d^e-axis and q^e-axis stator voltages, and λ_{ds}^e and λ_{qs}^e are the d^e-axis and q^e-axis stator fluxes, respectively. Moreover, R_s is the stator resistance, ω_e is the speed of the synchronous reference frame, and $p = d/dt$ represents the differential operator. Since the permanent magnet is located only on the d^e-axis, the d^e-axis and q^e-axis stator fluxes can be expressed as

$$\lambda_{ds}^e = L_s i_{ds}^e + \lambda_F , \tag{3}$$

$$\lambda_{qs}^e = L_s i_{qs}^e , \tag{4}$$

where λ_F is the equivalent flux of the rotor permanent magnet on the stator. By substituting Eqs. (3) and (4) into Eqs. (1) and (2), the two-axis stator current state matrix can be derived as

$$p\begin{bmatrix} i_{ds}^e \\ i_{qs}^e \end{bmatrix} = \begin{bmatrix} -R_s/L_s & \omega_e \\ -\omega_e & -R_s/L_s \end{bmatrix}\begin{bmatrix} i_{ds}^e \\ i_{qs}^e \end{bmatrix} + \frac{1}{L_s}\begin{bmatrix} v_{ds}^e \\ v_{qs}^e - \omega_e \lambda_F \end{bmatrix}. \tag{5}$$

In Eq. (5), an inspection of the right side of the first row reveals that the second term is a coupling component related to the q^e-axis stator current. Similarly, an inspection of the right side of the second row indicates that the first and fourth terms are coupling components associated with the d^e-axis stator current and the rotor equivalent flux, respectively. On the basis of these coupling components, the d^e-axis and q^e-axis stator voltage feed-forward compensations are defined as

$$\begin{bmatrix} v_{dsc}^e \\ v_{qsc}^e \end{bmatrix} = \begin{bmatrix} -\omega_e L_s i_{qs}^e \\ \omega_e L_s i_{ds}^e + \omega_e \lambda_F \end{bmatrix}. \tag{6}$$

The linear control of the d^e-axis and q^e-axis stator current control loops is derived and expressed as

$$p\begin{bmatrix} i_{ds}^{e} \\ i_{qs}^{e} \end{bmatrix} = \begin{bmatrix} -R_s/L_s & 0 \\ 0 & -R_s/L_s \end{bmatrix}\begin{bmatrix} i_{ds}^{e} \\ i_{qs}^{e} \end{bmatrix} + \frac{1}{L_s}\begin{bmatrix} v_{ds}^{e'} \\ v_{qs}^{e'} \end{bmatrix}, \tag{7}$$

where $v_{ds}^{e'}$ and $v_{qs}^{e'}$ are the outputs of the d^e-axis and q^e-axis stator current controllers, respectively. The voltage commands v_{ds}^{e*} and v_{qs}^{e*} for the d^e-axis and q^e-axis stator current control loops are given by

$$\begin{bmatrix} v_{ds}^{e*} \\ v_{qs}^{e*} \end{bmatrix} = \begin{bmatrix} v_{ds}^{e'} \\ v_{qs}^{e'} \end{bmatrix} + \begin{bmatrix} v_{dsc}^{e} \\ v_{qsc}^{e} \end{bmatrix}. \tag{8}$$

The developed electromagnetic torque and the mechanical equation of a PMSM are respectively expressed as

$$T_e = i_{qs}^{e}\lambda_F\,, \tag{9}$$

$$J_m p\omega_{rm} + B_m\omega_{rm} + T_L = T_e\,, \tag{10}$$

where J_m is the inertia of PMSM, B_m is the viscous friction coefficient, T_L is the load torque, $\omega_{rm} = (2/P)\omega_r$ is the mechanical speed of the motor shaft, P is the number of motor poles, and ω_r is the rotor electrical speed. As shown in Eq. (9), i_{qs}^{e} and λ_F are inherently orthogonal, enabling the achievement of the maximum torque-to-current ratio.

According to the first and second rows shown in Eq. (7), the plant models for the d^e-axis and q^e-axis stator current control loops are respectively derived as

$$G_{p\_i_{ds}^{e}}(s) = \frac{1/L_s}{s + R_s/L_s}\,, \tag{11}$$

$$G_{p\_i_{qs}^{e}}(s) = \frac{1/L_s}{s + R_s/L_s}\,, \tag{12}$$

where s is the Laplace operator. On the basis of Eq. (10) and defined $\Delta T_e = T_e - T_L$, the plant of the speed control loop is derived as

$$G_{p\_s}(s) = \frac{1/J_m}{s + B_m/J_m}\,. \tag{13}$$

The decoupled linear control block diagram of the FOC PMSM drive is shown in Fig. 1. Since the rotor poles are permanent magnets, the d^e-axis stator current command is set to $i_{ds}^{e*} = 0$. Here, (K_{ps}, K_{is}), (K_{pd}, K_{id}), and (K_{pq}, K_{iq}) are the proportional and integral gain parameter pairs for the speed, d^e-axis, and q^e-axis stator current controllers, respectively. The control gain of the internal control loop is much higher than that of the external control loop, allowing the closed-loop gain of the internal control loop to be regarded as unity. All controllers of the FOC PMSM drive were designed by the pole placement method.

Figure 2 illustrates the block diagram of the proposed FOC PMSM drive. This diagram includes a speed controller, d^e-axis and q^e-axis stator current controllers, d^e-axis and q^e-axis decoupling calculations, i_{qs}^{e*} calculation, and coordinate transformations between the three-phase system and the two-axis stationary reference frame ($2^s \Leftarrow 3$, $2^s \Rightarrow 3$). Here, the three-phase currents (i_{as}, i_{bs}, and i_{cs}) were obtained from the PMSM using electromagnetic Hall effect current sensors.

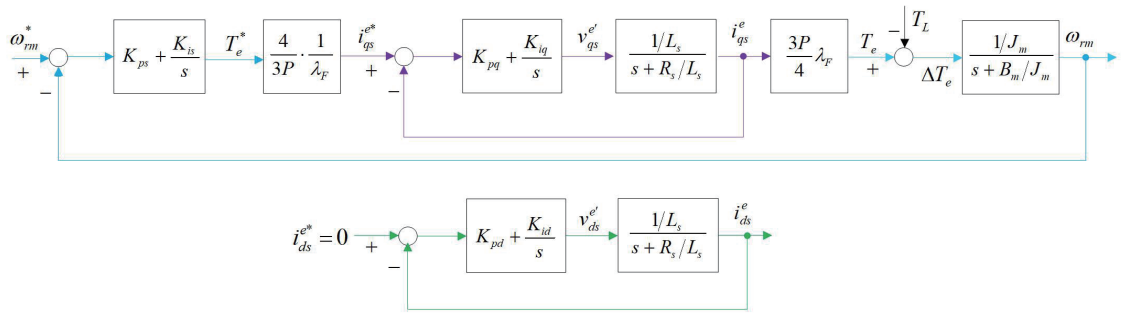

Fig. 1. (Color online) Decoupled linear control block diagram of FOC PMSM drive.

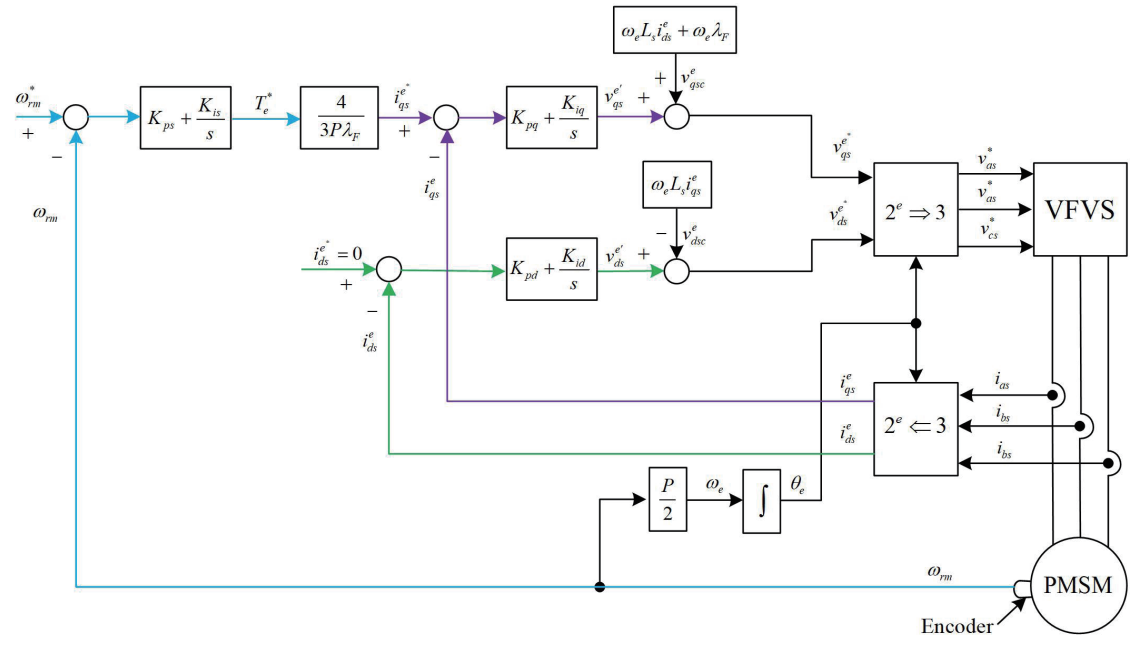

Fig. 2. (Color online) Block diagram of FOC PMSM drive.

3. APFC Bidirectional Power Flow Front-end Converter

An APFC bidirectional power flow front-end converter is developed, enabling the FOC PMSM drive to achieve unity power factor operation in both the motoring and regenerative braking modes. This enhances the power factor and contributes to energy savings.

The main circuit of the FOC PMSM drive with a front-end bidirectional power flow converter is shown in Fig. 3. In this circuit, an AC choke is employed for voltage boosting, filtering, and current storage. L represents the inductance of the AC choke, R is the internal resistance of the grid, C is the filter capacitance of the DC bus, v_{sg} and i_{sg} are the voltage and current of the grid, respectively, v_L is the AC choke voltage, and v_i is the pulse width modulation (PWM) power switch input voltage of the front-end converter.

On the basis of Fig. 3, the three-phase input voltages of the bidirectional power flow front-end converter are expressed as

$$v_a = Ri_{aG} + L \cdot pi_{aG} + v_{an}, \tag{14}$$

$$v_b = Ri_{bG} + L \cdot pi_{bG} + v_{bn}, \tag{15}$$

$$v_c = Ri_{cG} + L \cdot pi_{cG} + v_{cn}, \tag{16}$$

where v_a, v_b, and v_c are the three-phase voltages, i_{aG}, i_{bG}, and i_{cG} are the three-phase currents, and v_{an}, v_{bn}, and v_{cn} are the three-phase neutral voltages on the grid side.

When the PMSM operates in motoring mode, the PWM power switch of the front-end converter converts the grid-side AC voltage into a DC voltage for the DC bus, while the PWM power switch of the motor inverter converts the DC voltage from the DC bus into a variable-frequency AC voltage for the PMSM. Conversely, when the PMSM operates in regenerative braking mode, the anti-parallel flywheel diodes in the PWM power switch of the motor inverter channel the braking regenerative energy from the PMSM to the DC bus. The PWM power switch of the front-end converter then converts the DC voltage from the DC bus into a rated-frequency AC voltage for the grid side.

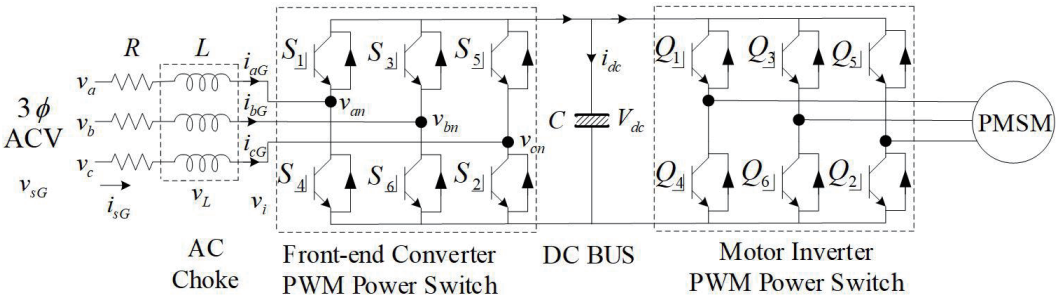

Fig. 3. Front-end converter and motor inverter PWM power switches.

According to the PFC theory,[23] in order to maintain unity power factor operation during both the motoring and regenerative braking modes, the vector relationship between the voltage and current of the front-end converter is as illustrated in Fig. 4. In motoring mode, the control variable v_i is adjusted to ensure a 0° phase relationship between v_{sg} and i_{sg}, as shown in Fig. 4(a). Similarly, in regenerative braking mode, v_i is adjusted to maintain a 180° phase relationship between v_{sg} and i_{sg}, as shown in Fig. 4(b).

On the basis of Eqs. (14)–(16), and by applying the grid-side coordinate transformation from the three-phase frame to the two-axis synchronous reference frame, the two-axis voltage equations of the front-end converter in the synchronous reference frame are expressed as[23]

$$(L \cdot p + R) i_{dG}^{e} = v_{dG}^{e} - v_{dn}^{e} + \omega_G L i_{qG}^{e}, \tag{17}$$

$$(L \cdot p + R) i_{qG}^{e} = v_{qG}^{e} - v_{qn}^{e} - \omega_G L i_{dG}^{e}, \tag{18}$$

where v_{dG}^{e} and i_{dG}^{e} are the d_G^e-axis voltage and current, v_{qG}^{e} and i_{qG}^{e} are the q_G^e-axis voltage and current, v_{dn}^{e} and v_{qn}^{e} are the d_G^e-axis and q_G^e-axis neutral voltages on the grid side, respectively, and ω_G is the speed of the grid-side synchronous reference frame. The left sides of Eqs. (17) and (18) are respectively defined as

$$v_{dG}^{e'} = v_{dG}^{e} - v_{dn}^{e} + \omega_G L i_{qG}^{e}, \tag{19}$$

$$v_{qG}^{e'} = v_{qG}^{e} - v_{qn}^{e} - \omega_G L i_{dG}^{e}. \tag{20}$$

By substituting Eqs. (19) and (20) into Eqs. (17) and (18), respectively, and applying feedforward voltage compensation, the plant models of the d_G^e-axis and q_G^e-axis current controllers for the front-end converter can be derived as

$$\frac{i_{dG}^{e}}{v_{dG}^{e'}} = \frac{1/L}{s + R/L}, \tag{21}$$

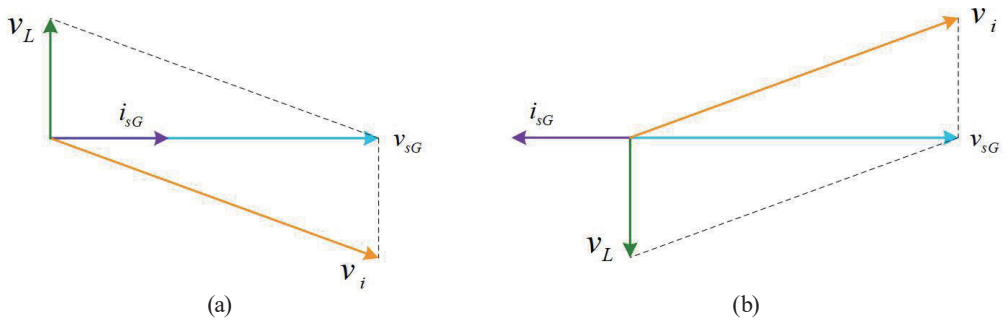

Fig. 4. (Color online) Vector relationship between v_{sG} and i_{sG} of the front-end converter. (a) Motoring. (b) Regenerative braking.

$$\frac{i_{qG}^{e}}{v_{qG}^{e'}} = \frac{1/L}{s + R/L}, \tag{22}$$

where $v_{dG}^{e'}$ and $v_{qG}^{e'}$ are the outputs of the d_G^e-axis and q_G^e-axis current controllers of the front-end converter, respectively.

The d_G^e-axis and q_G^e-axis current control loops of the front-end converter are expressed as

$$v_{dG}^{e'} = (K_{pdG} + \frac{K_{idG}}{s})(i_{dG}^{e^*} - i_{dG}^{e}), \tag{23}$$

$$v_{qG}^{e'} = (K_{pqG} + \frac{K_{iqG}}{s})(i_{qG}^{e^*} - i_{qG}^{e}), \tag{24}$$

where $i_{dG}^{e^*}$ and $i_{qG}^{e^*}$ are the d_G^e-axis and q_G^e-axis current commands of the front-end converter, and (K_{pdG}, K_{idG}) and (K_{pqG}, K_{iqG}) are the proportional and integral gain parameter pairs for the d_G^e-axis and q_G^e-axis current controllers of the front-end converter, respectively. The voltage commands of the d_G^e-axis and q_G^e-axis current control loops of the front-end converter are expressed as

$$v_{dG}^{e^*} = v_{dG}^{e'} + v_{dG}^{e} - \omega_G L i_{qG}^{e}, \tag{25}$$

$$v_{qG}^{e^*} = v_{qG}^{e'} + v_{qG}^{e} + \omega_G L i_{dG}^{e}. \tag{26}$$

The three-phase grid-side voltage in the two-axis synchronous reference frame is derived as

$$v_{dG}^{e} = 0, \tag{27}$$

$$v_{qG}^{e} = -V_m, \tag{28}$$

where V_m is the instantaneous maximum of the three-phase voltage on the grid side. Furthermore, the three-phase grid-side current in the two-axis synchronous reference frame is derived as

$$i_{dG}^{e} = -I_m \sin\theta, \tag{29}$$

$$i_{qG}^{e} = -I_m \cos\theta, \tag{30}$$

where I_m is the instantaneous maximum of the three-phase grid-side current, and θ is the phase angle between the voltage and current on the grid side. The active power and reactance power of the grid side in the synchronous reference frame are respectively derived as

$$P_G = (3/2)(v_{qG}^e i_{qG}^e + v_{dG}^e i_{dG}^e), \tag{31}$$

$$Q_G = (3/2)(v_{qG}^e i_{dG}^e - v_{dG}^e i_{qG}^e). \tag{32}$$

On the basis of Eqs. (27) and (28), Eqs. (31) and (32) can be rewritten as

$$P_G = (3/2)(-V_m i_{qG}^e), \tag{33}$$

$$Q_G = (3/2)(-V_m i_{dG}^e). \tag{34}$$

As shown in Eqs (33) and (34), if V_m is a constant, P_G and i_{qG}^e are linearly related, and Q_G and i_{dG}^e are also linearly related. Specifically, by setting $i_{dG}^e = 0$, it follows that $Q_G = 0$, enabling the bidirectional power flow front-end converter to operate close to unity power factor.

The control block diagram of the bidirectional power flow front-end converter with APFC is shown in Fig. 5. Here, V_{dc}^* and V_{dc} represent the reference and actual voltages of the DC bus, while i_{qG}^{e*} and i_{dG}^{e*} are the reference currents for the grid q_G^e-axis and d_G^e-axis, respectively. Unity power factor operation is achieved by setting $i_{dG}^{e*} = 0$. Additionally, v_{qG}^* and v_{dG}^* are the outputs of the i_{qG}^e- and i_{dG}^e-controllers, respectively. The trigger signals for the front-end converter's PWM power switch are generated from v_{qG}^* and v_{dG}^* through the modulator. All three controllers are proportional–integral (P–I) types and were designed using root locus and Bode plot techniques. Furthermore, the two-axis grid currents (i_{qG}^e and i_{dG}^e) were obtained from the grid using electromagnetic Hall effect current sensors and transformed from the three-phase frame to the two-axis synchronous reference frame. The actual DC bus voltage V_{dc} was measured using a voltage-dividing isolation sensor.

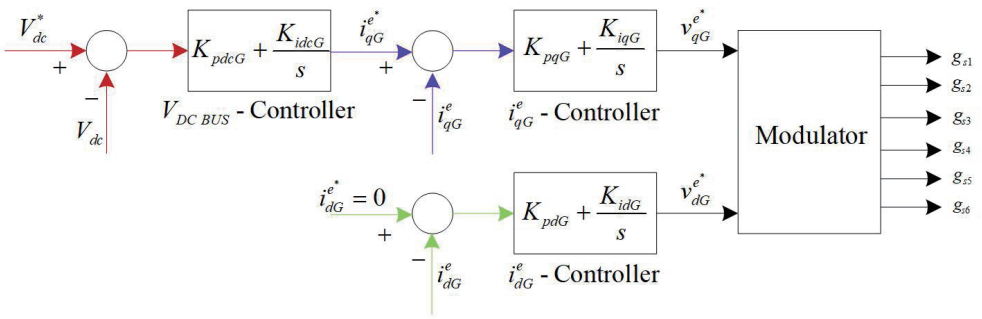

Fig. 5. (Color online) APFC bidirectional power flow front-end converter control block diagram.

4. Simulation Setup and Results

A three-phase, 220 V, 0.75 kW, Y-connected PMSM was used as the controlled plant for experimentation to validate the effectiveness of the proposed FOC PMSM drive with APFC. The motor speed command during a running cycle was designed as follows: forward acceleration from $t = 0$ to $t = 1$ s, forward steady-state running over $1 \leq t \leq 3$ s, forward braking to reach zero speed within the interval $3 \leq t \leq 4$ s, reverse acceleration from $t = 4$ to $t = 5$ s, reverse steady-state running over $5 \leq t \leq 7$ s, and reverse braking to reach zero speed within the interval $7 \leq t \leq 8$ s. The simulated and experimental results of the proposed FOC PMSM drive under a load of 2 N-m for reversible steady-state speed commands at 1500 rev/min during the first two running cycles are shown in Figs. 6 and 7, respectively. Each figure illustrates four responses: (a) command (dashed line) and actual (solid line) rotor speed, (b) q^e-axis stator current, (c) electromagnetic torque, and (d) synchronous position angle.

The simulated and experimental results for the phase-a voltage and current of the bidirectional power flow front-end converter in the proposed FOC PMSM drive with APFC during motoring

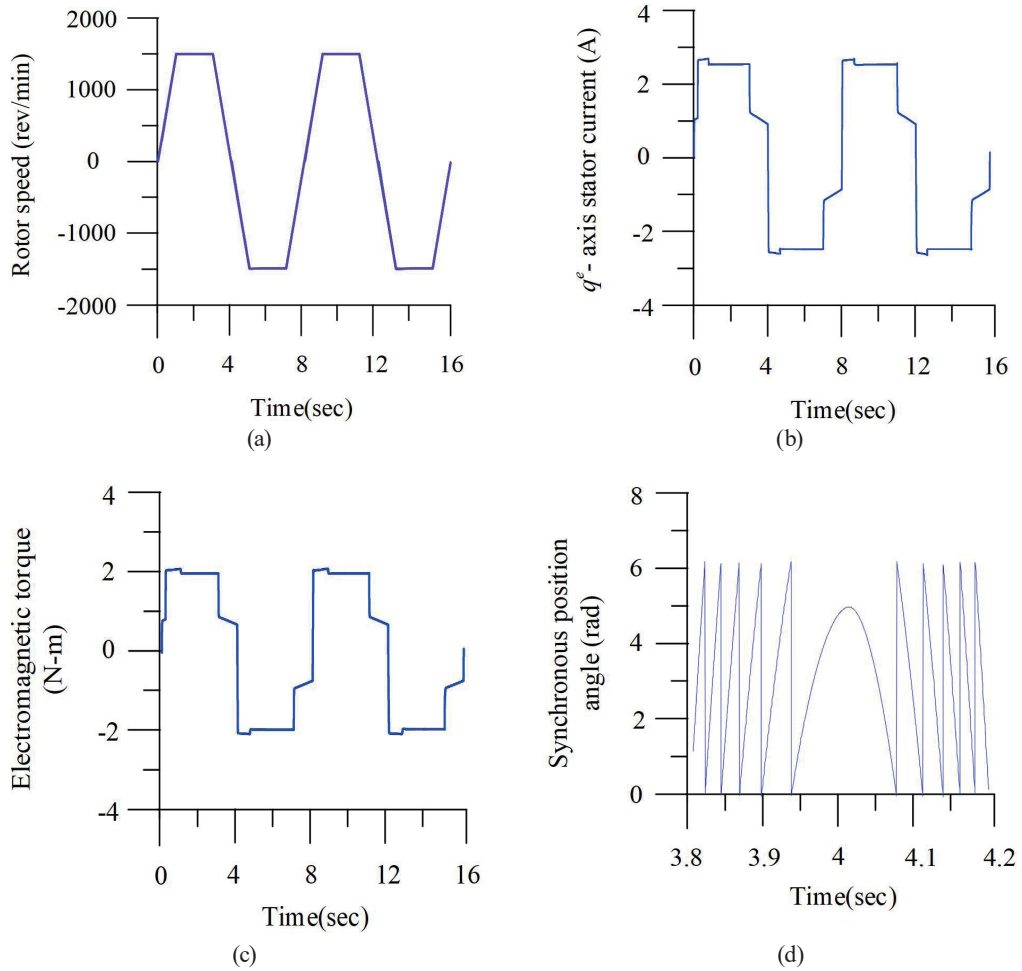

Fig. 6. (Color online) Simulated results of the proposed FOC PMSM drive with a load of 2 N-m for a reversible steady-state speed command of 1500 rev/min: (a) rotor speed, (b) q^e-axis stator current, (c) electromagnetic torque, and (d) synchronous position angle.

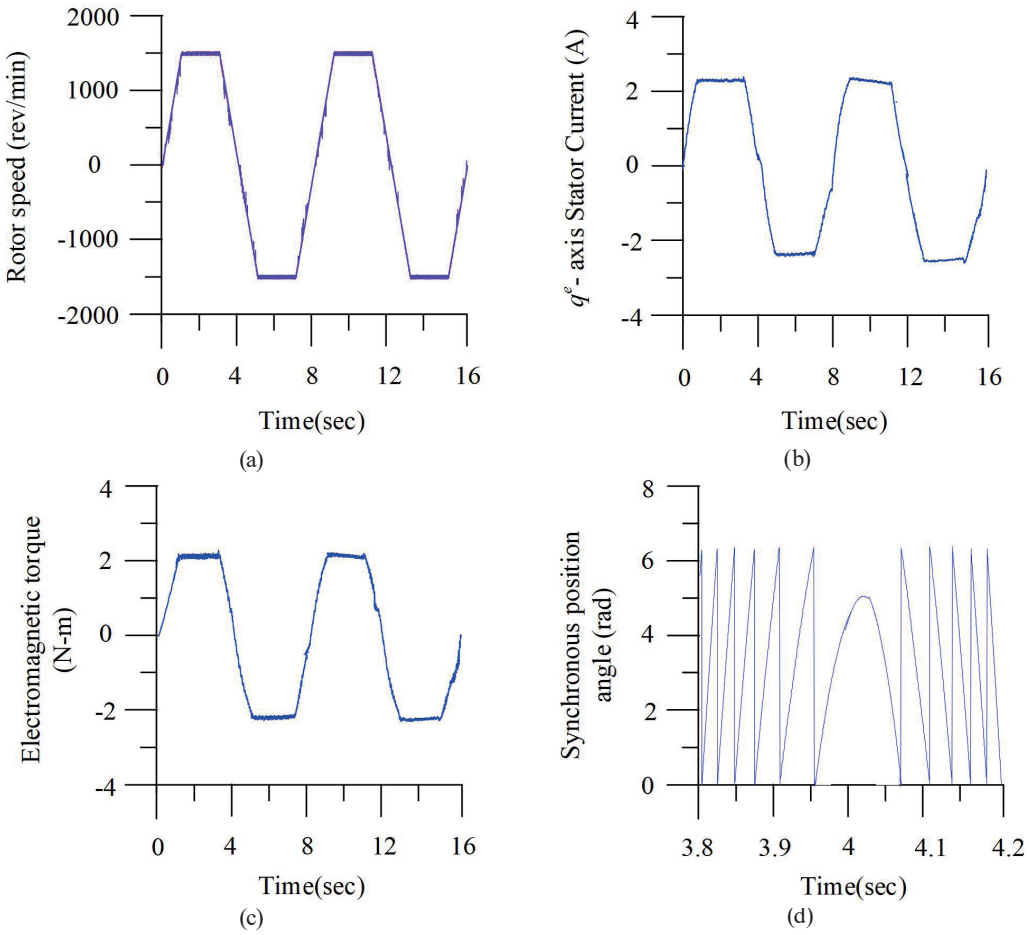

Fig. 7. (Color online) Experimental results of the proposed FOC PMSM drive with a load of 2 N-m for a reversible steady-state speed command of 1500 rev/min: (a) rotor speed, (b) q^e-axis stator current, (c) electromagnetic torque, and (d) synchronous position angle.

and regenerative braking operations are presented in Figs. 8 and 9, respectively. Each figure includes two responses: (a) simulated and (b) experimental results. Specifically, Fig. 8 shows the phase-a voltage and current of the APFC bidirectional power flow front-end converter during motoring operation, while Fig. 9 illustrates the corresponding results during regenerative braking operation.

On the basis of the simulated and experimental results observed in the reversible transient and steady-state operations of the FOC PMSM drive, the rotor speed was accurately obtained. The q^e-axis stator current and electromagnetic torque responses confirmed the loading effect. The sawtooth pattern of the estimated synchronous position angle validated the accuracy of the coordinate transformation between the synchronous and stationary reference frames. Furthermore, the analysis of the simulated and experimental results for the phase-a voltage and current of the APFC bidirectional power flow front-end converter during motoring and regenerative braking confirmed that unity power factor operation was achieved. Therefore, the developed FOC PMSM drive with APFC has demonstrated the capability to achieve the desired performance.

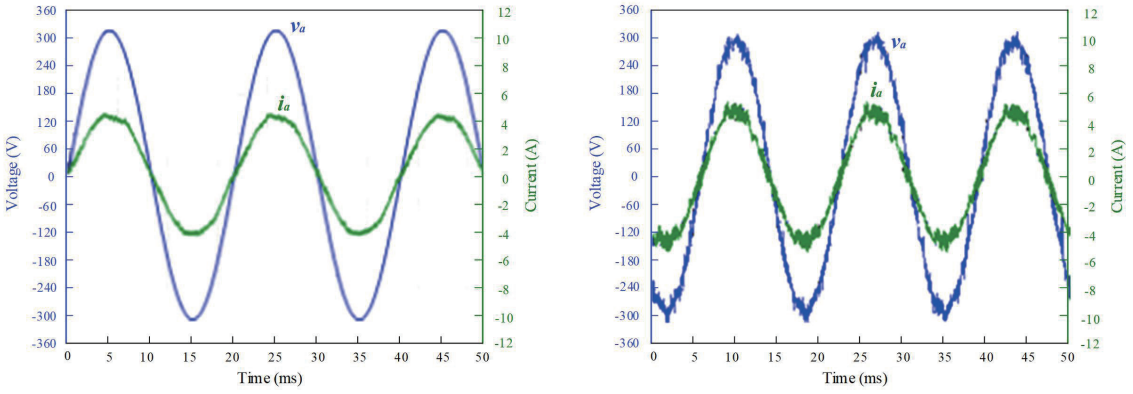

Fig. 8. (Color online) Phase-a voltage and current of the bidirectional power flow front-end converter in the proposed FOC PMSM drive with APFC during motoring operation: (a) simulated result and (b) experimental result.

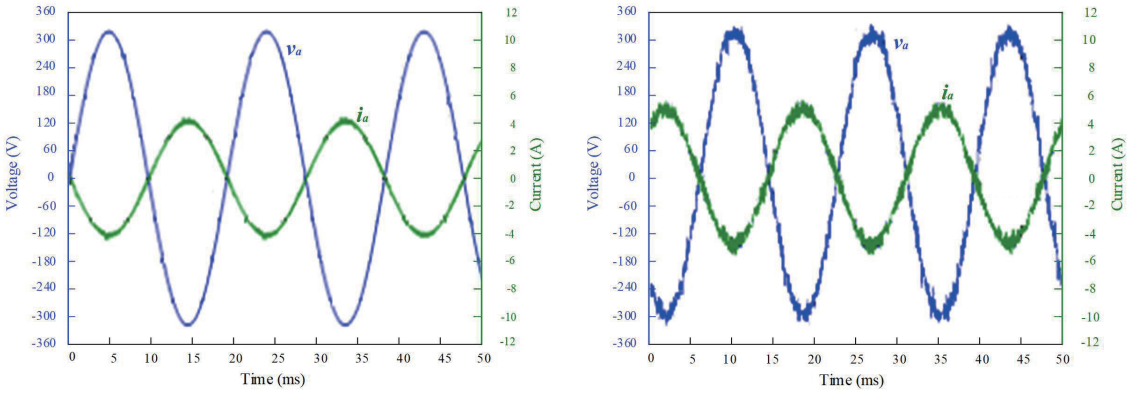

Fig. 9. (Color online) Phase-a voltage and current of the bidirectional power flow front-end converter in the proposed FOC PMSM drive with APFC during regenerative braking operation: (a) simulated and (b) experimental results.

5. Conclusions

An APFC bidirectional power flow front-end converter was developed for the FOC PMSM drive. The decoupled FOC PMSM drive was designed on the basis of the stator current and flux, achieving linear controller implementation using stator voltage feed-forward compensation and obtaining the maximum torque-to-current ratio. The developed APFC bidirectional power flow front-end converter enabled the FOC PMSM drive to maintain unity power factor operation during both motoring and regenerative braking. The three-phase current measurements required for implementing the FOC PMSM drive with APFC were acquired using Hall effect current sensors. Simulation and experimental results for reversible steady-state speed commands under load conditions, as well as the phase-a voltage and current of the front-end converter during motoring and regenerative braking operations, confirmed the promising performance of the proposed FOC PMSM drive with APFC.

References

1 Y. C. Luo, S. Y. Xie, C. H. Lin, and Y. P. Kuo: Sens. Mater. **35** (2023) 2101. https://doi.org/10.18494/SAM.4290
2 T. M. Parreiras, J. C. G. Justino, A. V. Rocha, and B. J. C. Filho: IEEE Trans. Ind. Appl. **52** (2016) 2737. https://doi.org/10.1109/TIA.2016.2533499
3 V. P. Mini, N. Mayadevi, R. H. Kumar, and C. Gopal: Proc. 2017 Int. Intelligent Computing, Instrumentation and Control Technologies Conf. (ICICICT, 2017) 665–672. https://doi.org/10.1109/ICICICT1.2017.8342642
4 B. Singh, G. Bhuvaneswari, and S. Madishetti: Proc. 2011 Int. Power and Energy Systems Conf. (IPES, 2011) 1–6. https://doi.org/10.1109/ICPES.2011.6156685
5 S. Sajeev and A. Mathew: Proc. 2013 Int. Emerging Trends Communication, Control, Signal Processing and Computing Applications Conf. (C2SPCA, 2013) 1–6. https://doi.org/10.1109/C2SPCA.2013.6749436
6 V. Bist and B. Singh: IEEE Trans. Ind. Electron. **62** (2015) 4118. https://doi.org/10.1109/TIE.2014.2384001
7 B. Singh and V. Bist: IEEE Trans. Ind. Electron. **62** (2015) 172. https://doi.org/10.1109/TIE.2014.2327551
8 V. Bist and B. Singh: IEEE Trans. Ind. Inf. **10** (2014) 1207. https://doi.org/10.1109/TII.2014.2305620
9 P. K. Singh B. Singh, V. Bist, K. A. Haddad, and A. Chandra: IEEE Trans. Ind. Appl. **54** (2018) 625. https://doi.org/10.1109/TIA.2017.2740281
10 A. Kumar and B. Singh: IEEE J. Emerging Sel. Top. Ind. Electron. **5** (2024) 1666. https://doi.org/10.1109/JESTIE.2024.3391334
11 S. Ranjit, A. Arya, B. Saha, S. Kumar, and B. Singh: Proc. 2023 IEEE 3rd Int. Smart Technologies Power, Energy and Control Conf. (STPEC, 2023) 1–6. https://doi.org/10.1109/STPEC59253.2023.10431099
12 K. A. Singh, A. Chaudhary, and K. Chaudhary: J. Mod. Power Syst. Clean Energy **11** (2023) 589. https://doi.org/10.35833/MPCE.2022.000060
13 K. Biswas, O. Ray, and C. N. Bhende: Proc. 2023 11th Int. National Power Electronics Conf. (NPEC, 2023) 1–6. https://doi.org/10.1109/NPEC57805.2023.10384963
14 C. C. Lin and Y. Y. Tzou: Proc. 2014 IEEE Energy Conversion Congress and Exposition Conf. (ECCE, 2014) 1476–1481. https://doi.org/10.1109/ECCE.2014.6953593
15 M. Elmi, R. Alizadeh, and A. Ajami: Proc. 2015 6th Power Electronics, Drive Systems & Technologies Conf. (PEDSTC2015) 1476–1481. https://doi.org/10.1109/PEDSTC.2015.7093275
16 Y. Tang, Y. He, F. Wang, G. Lin, J. Rodríguez, and R. Kennel: IEEE Trans. Energy Convers. **36** (2021) 2163. https://doi.org/10.1109/TEC.2021.3051167
17 A. Anand and B. Singh: IEEE Trans. Power Electron. **34** (2019) 624. https://doi.org/10.1109/TPEL.2018.2827048
18 M. Mohamadi, A. Rashidi, S. M. S. Nejad, and M. Ebrahimi: IEEE Trans. Ind. Electron. **65** (2018) 8330. https://doi.org/10.1109/TIE.2017.2787553
19 Y. He, Y. Tang, H. Xie, F. Wang, J. Rodriguez, and R. Kennel: IEEE Trans. Energy Convers. **38** (2023) 519. https://doi.org/10.1109/TEC.2022.3203626
20 H. C. Chang and C. M. Liaw: IEEE Trans. Ind. Electron. **58** (2011) 1763. https://doi.org/10.1109/TIE.2010.2051938
21 H. Cheng, L. Wang, L. Xu, X. Ge, and S. Yang: IEEE Trans. Ind. Electron. **67** (2020) 8231. https://doi.org/10.1109/TIE.2019.2947854
22 C. H. Liu: Control of AC Electrical Machines (Tunghua, Taipei, 2008) 4th ed., Chap. 6 (in Chinese).
23 T. Friedli, M. Hartmann, and J. W. Kolar: IEEE Trans. Power Electron. **29** (2014) 543. https://doi.org/10.1109/TPEL.2013.2258472